# CREEP AND CREEP-FATIGUE BEHAVIOR OF AN ADVANCED STAINLESS STEEL (ALLOY 709) - APPLICATION TO SODIUM-COOLED FAST REACTORS

ABDULLAH S. ALOMARI [1,2]*, ZEINAB ALSMADI [2], NILESH KUMAR [2,3], K.L. MURTY [2]

[1]Nuclear Science Research Institute, King Abdulaziz City for Science and Technology, Riyadh, Saudi Arabia.
[2]Department of Nuclear Engineering, North Carolina State University, Raleigh, NC, USA.
[3]Metallurgical and Materials Engineering, The University of Alabama, Tuscaloosa, AL, USA.

*Email contact of corresponding author: asalomari@kacst.edu.sa

## ABSTRACT

Sodium-cooled Fast Reactor (SFR) possesses highest technology readiness level for deployment among six Gen-IV nuclear reactor designs intended to provide a low-carbon energy option and endure higher operating temperatures for longer service life (60-80 years). Thus, advanced materials developed for Gen-IV reactors should be able to withstand the harsh operating conditions allowing for safety improvement, efficiency enhancement and cost reduction. The advanced austenitic stainless-steel Alloy 709 (Fe-25wt.%Ni-20%Cr) is of current interest for structural applications in the SFRs owing to its desired set of properties including mechanical properties relative to conventional austenitic stainless steels. SFRs are subjected to on-load periods at elevated temperatures and thermal transients during startups and shutdowns, resulting in creep, fatigue, and creep-fatigue interaction as major considerations in the design of such high-temperature systems. In this work, high-temperature creep, fatigue and creep-fatigue behavior of the Alloy 709 are characterized along with microstructural examinations before and after mechanical testing. Creep tests were carried out at temperatures and stresses from 700 – 800 °C and 40 – 275 MPa, respectively, and the creep data were found to follow creep-power law with true stress exponent and activation energy of 4.9 ± 0.2 and 299 ± 15 kJ/mole, respectively. The microstructural observations of the crept specimens revealed different types of precipitates including Z-phases and the evidence of dislocation-precipitate interactions together with subgrain boundary formation. This suggests that high-temperature dislocation climb deformation is the rate-controlling creep mechanism in the alloy. Additionally, Larson-Miller Parameter (LMP) and Monkman–Grant relationships were developed using the creep rupture data.

## 1. INTRODUCTION

Towards achieving the worldwide goals of decreasing carbo dioxide emissions and meeting the increased demand for electricity, next-generation nuclear reactors (Gen-IV reactors) are expected to be the primary source of baseload power in many countries within next decades [1]. However, the increase demand in their operation condition relative to the current fleet of nuclear reactors such as higher operating temperatures, longer lasting, harsher environment and high dose of radiation, put forward several technical challenges for deployment which need to be addressed for safer, more reliable, economically viable and sustainable operation [2]. Sodium-cooled Fast reactor (SFR) is one of the leading advanced nuclear reactor systems and most ready for deployment among other Gen-IV reactor concepts mainly due to large worldwide experiences accumulated over more than 40 years [3]. SFRs can provide a low-carbon energy option to a diverse global power sources and support other missions such as recycling the used nuclear fuel for closing the fuel cycle. The main challenges facing the SFRs technologies are the insufficient plant availability and high capital cost of deployment [4]. Thus, advanced structural materials with improved performance are needed for SFRs to enhance thermal efficiency, power output and design lifetimes of the reactor components and to enable greater safety margins [3, 5]. Although the operating temperature of the SFRs can reach as high as 550 °C, the service temperature for some structural components such as boiler tubes can be exposed to higher service temperatures and thus, exhibit shorter lifetimes.

The Alloy 709 is an advanced austenitic stainless steel with base of Fe-20%Cr-25%Ni (wt.%) strengthened by niobium, stabilized by nitrogen and alloyed with other minor elements. Due to various improved properties including excellent high temperature creep performance coupled with corrosion/oxidation resistance and sodium compatibilities relative to code-approved conventional steels such as 304SS and 316SS, the Alloy 709 has been down-selected for SFR structural applications [6-10]. Several studies have been recently conducted to understand

the performance of the Alloy 709 at high temperatures such as effect of serrated yielding on mechanical performance and microstructures [11], tensile behaviour [12-15], creep and creep-fatigue properties [13, 16-23], effect of irradiation and aging on microstructures [24-27], elastic characterises [28] and thermophysical properties [29]. However, understanding high temperature deformation properties of the Alloy 709 are required to incorporate such a new alloy in the ASME Boiler and Pressure code for reliable operation [30]. Specifically, understanding creep and creep-fatigue interactions behaviour are essential for structural component operating under cyclic and steady-state conditions. Therefore, it is important to investigate and understand the creep and creep-fatigue interaction of the Alloy 709 at higher temperatures to generate enough amount of data in a reasonable time and then extrapolate it to the service conditions expected in SFRs. Although some works have been found in the literature to examine the behaviour of the Alloy 709 under creep-fatigue testing, the details mechanism are still scarce. In this study, creep tests were carried out at temperatures ranging from 650 – 800 °C and creep-fatigue tests were carried out under strain-controlled mode at constant strain rate of $2 \times 10^{-3}$ $s^{-1}$ and strain ranges varying from 0.3% to 1.2% at temperatures of 650 °C and 750 °C with tensile hold times of 0, 60, 600, 1,800, and 3,600 seconds. Tests were followed by microstructural examination in order to infer the deformation micromechanisms under such conditions.

## 2. EXPERIMENTAL METHODS AND MATERIAL

The Alloy 709 employed in this study has the chemical composition listed in TABLE 1. For creep tests, rectangular pin-loaded samples were prepared with of 25.4 mm × 1.2 mm × 6.3 (gage lengths × thickness × width, respectively) while cylindrical samples of 3 mm diameter gage section and 10 mm length were employed for creep-fatigue tests. The experimental set-up for both creep and creep-fatigue tests are shown in Fig. 1 where constant load lever arm machine (Fig. 1a) was used for creep tests and electrodynamic TestResources machine (Model 810LE3) was employed for creep-fatigue tests (Fig. 1b). Details description for the experimental set-up can be found elsewhere [16]. Creep tests were carried out at temperatures and stresses from 700 – 800 °C and 40 – 275 MPa.

TABLE 1. CHEMICAL COMPOSITION (WT%) OF ALLOY 709 USED IN THIS WORK.

| Element | Fe | Ni | Cr | Mo | Mn | Si | Nb | N | C | Ti | P | B | S |
|---|---|---|---|---|---|---|---|---|---|---|---|---|---|
| wt% | Bal. | 24.98 | 19.93 | 1.51 | 0.91 | 0.44 | 0.26 | 0.148 | 0.07 | 0.04 | <0.014 | 0.0045 | <0.001 |

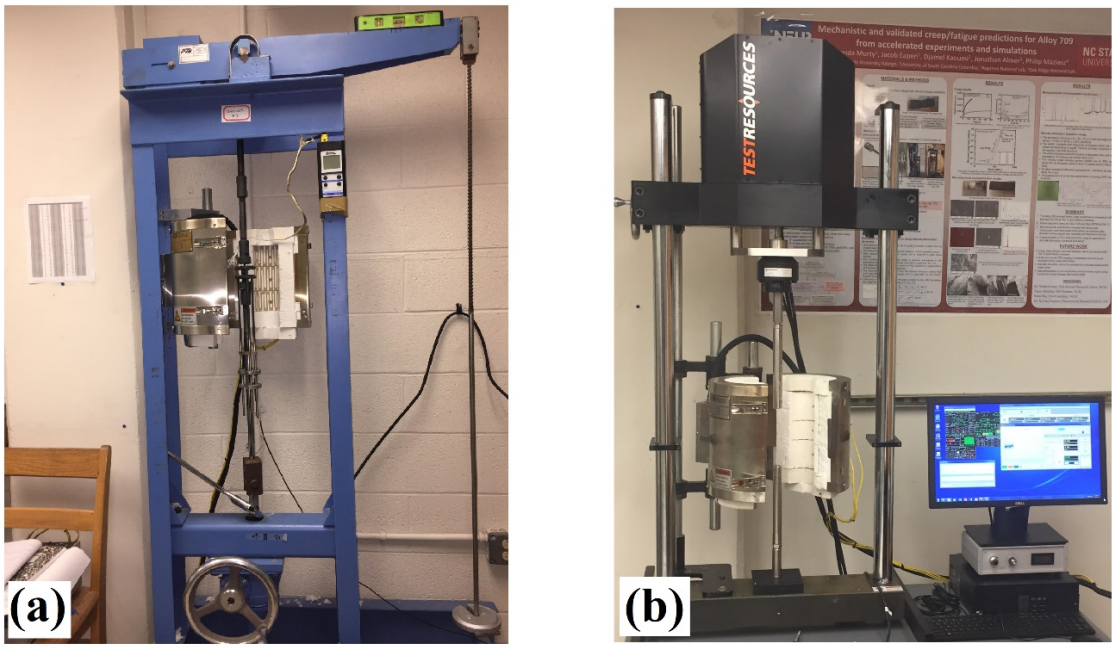


*FIG.1 (a) Constant load lever arm creep machine. (b) Electrodynamic TestResources creep-fatigue machine (Model 810LE3) was employed for creep-fatigue tests*

## 3. RESULTS AND DISCUSSIONS

### 3.1. High-temperature Creep Deformation

#### 3.1.1. Creep Curves and Deformation Mechanisms in The Alloy709

Creep strain as function of the time at applied stresses ranging from 40 – 275 MPa and temperatures of 700 °C, 750 °C and 800 °C are shown in FIG.2 for the Alloy 709. Typical creep curves exhibiting the three regimes of primary, steady state and tertiary creep regimes were usually observed in the Alloy 709. Theoretically, the primary regime is resulting from the increase in the hardening rate relative to the recovery process leading to the increase in the creep rate. As the recovery rate at high temperatures becomes equal to the hardening rate, steady state regime is formed where the creep rate is a constant as function of time. Finally, the sample enter the tertiary regime where increase in the creep rate keeps going until fracture due to various fracture process including creep cavities etc. The steady state creep region is of importance because the steady state creep rate corresponds to the minimum creep rate which is a unique function of the stress and temperature. Further, the minimum creep rate is also function of the time to rupture for most materials. To determine the steady state creep rate, one can differentiate the creep strain as function of time and then determine the minimum creep rate. Typical creep strain rate versus time at temperatures of 750 °C showing the values of the minimum creep rate at various stresses is shown in FIG.3. For high stresses where the tests were performed up to rupture, minimum creep rate can be defined as the point of deflection to the tertiary regime. At low stresses however, the tests were interrupted in the steady state region and the values of the steady state creep rates were employed. The minimum creep rate, $\dot{\varepsilon}_m$ and applied stress, σ can be related by a power law relation as follow,

$$\dot{\varepsilon}_m = A\sigma^n \exp\left(-\frac{Q_c}{RT}\right), \tag{1}$$

where $n$ the stress exponent, $Q_c$ the activation energy for creep, $R$ the universal gas constant and $T$ the temperature. The stress exponent and the activation energy for creep are considered to be indicative parameters to infer the rate controlling creep mechanism. FIG.4 shows the minimum creep rate versus applied stress at various temperature in log-log scale where an average value of the stress exponent was found to be 7.1 ± 0.6. To determine the activation energy, semi-log plot of the minimum creep rate versus the reciprocal temperature at various applied stresses was plotted in FIG.4 and a value of the 446 kJ/mole for the activation energy for creep in the Alloy 709 was obtained. The value of stress exponent for the Alloy 709 was found be similar to those obtained for other austenitic stainless steels [9, 16]. The values of stress exponent between 3-7 suggests that dislocation creep is the rate controlling creep mechanism in this level of stresses and temperatures. For pure metals and class-M alloys the activation energy is found to be close to that of self-diffusion or solute-diffusion depending on the rate controlling dislocation motion either climb or glide process respectively [5]. However, in the Alloy 709, the activation energy was found to be relatively higher activation energy relative to the self-diffusion of iron (~285 kJ/mole). This high anomalous value may originate from the interaction between the dislocation and precipitate during glide and climb processes in precipitation of hardened alloys. During deformation, various types of precipitates are formed in the Alloy 709 which can act as pinning obstacles for the moving dislocations [16].

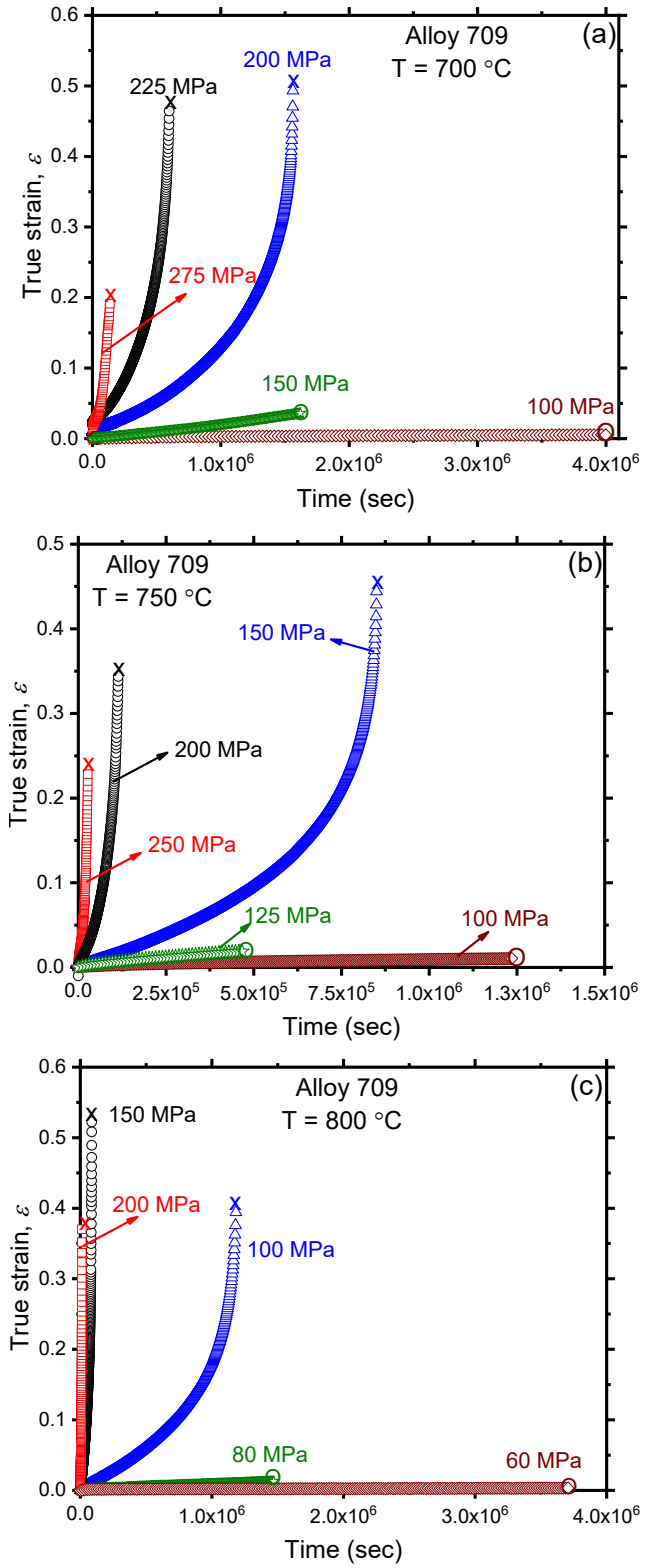


FIG.2 Creep true strain versus time at various applied stresses and temperatures of (a) 700 °C, (b) 750 °C and (c) 800 °C. X: sample ruptured. O: test interrupted.

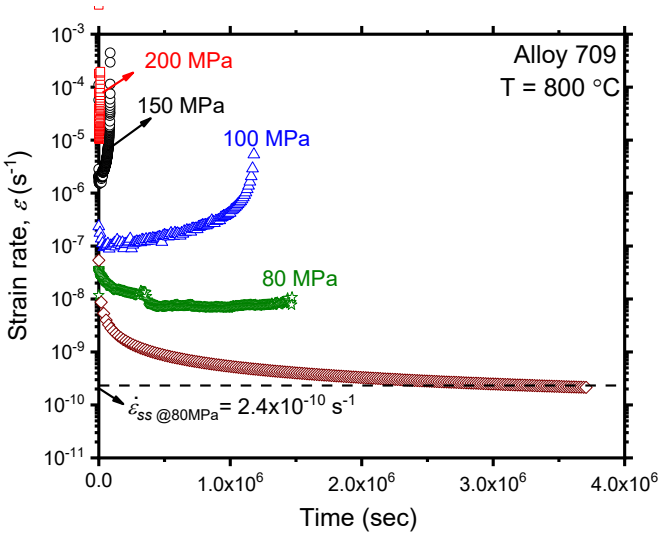


FIG.3 Typical creep strain rate versus time at temperatures of 750 °C showing the values of the minimum creep rate at various stresses.

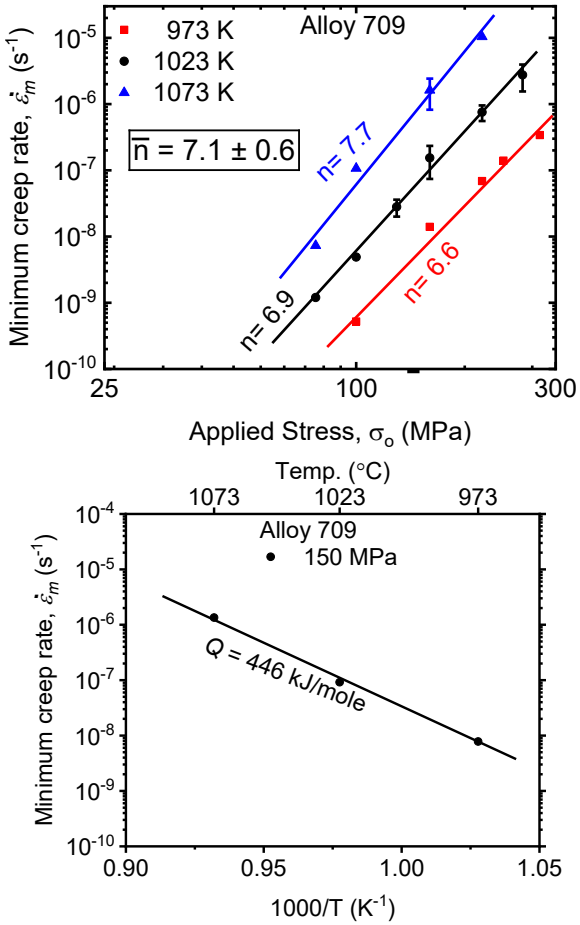


FIG.4 The minimum creep rate versus applied stress at various temperature in log-log scale (up). Determination the activation energy using Semilog plot of the minimum creep rate versus the reciprocal temperature at various applied stresses (below).

3.1.2. Larson-Miller Parameter (LMP) and Monkman–Grant relationships

To establish the Monkman-Grant relation for the Alloy 709, the variation of the creep life $t_f$ as function of the minimum creep rate at different temperatures is shown in FIG.5. The Alloy 709 was observed to flow the Monkman-Grant relation expressed as,

$$\dot{\varepsilon}_m^{\alpha}\ t_f = C_{MG}\,, \tag{2}$$

where α and $C_{MG}$ are constants. In this alloy, α and C are determined to be close to 1 and 0.1, respectively. Further, the applicability of the Larson– Miller parameter (LM) for the Alloy was demonstrated using the relation between creep life and the applied stress, as

$$LMP = T\,.\left[C + \log\left(t_f\right)\right], \tag{3}$$

where the temperature T is in K, the creep life, $t_f$ in hr and C is a constant found to be ~ 20. The applied stress vs LMP at different temperatures are shown in FIG.6 where LMP parameters were observed to be independent of the temperature at a given stress. The estimated temperatures in K for 100,000 hours rupture life using LMP are also shown in the top x-axis FIG.6

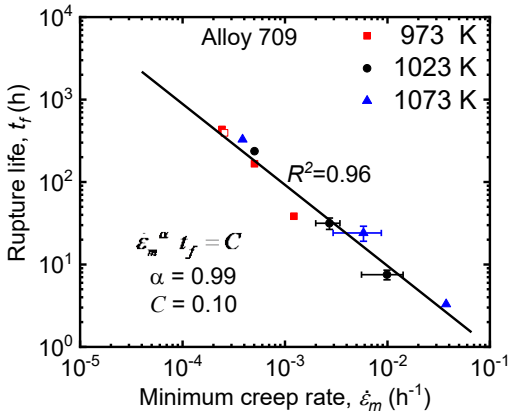


FIG.5 Establishing the Monkman-Grant relation for the Alloy 709.

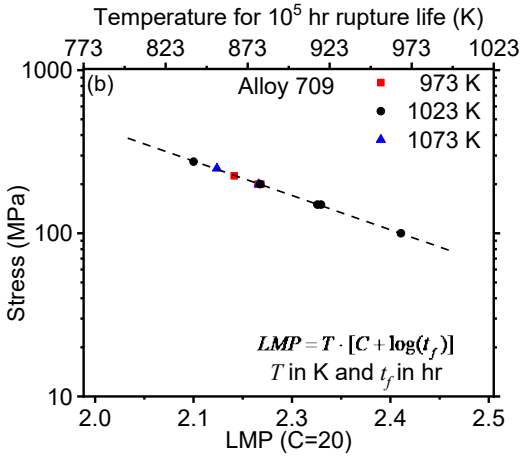


FIG.6 Establishing the Larson–Miller parameter (LMP) plot at different temperatures for the Alloy 709.

### 3.2. High-Temperature Creep-Fatigue Behavior of The Alloy 709

3.2.1. Creep-Fatigue Life of The Alloy 709

Strain-controlled creep-fatigue tests were performed on the Alloy 709 at 650 °C and 750 °C and $2\times10^{-3}$ $s^{-1}$ strain rate with strain ranging from 0.3% to 1.2% and tensile hold times of 0, 60, 600, 1,800, and 3,600 seconds. As shown in FIG.7, the creep-fatigue life of the Alloy 709 was found to decrease with increasing hold time (FIG.7a), strain range (FIG.7b) and temperature (FIG.7c), until it reached saturation where number of cycles to failure does not change with increasing hold time or strain range at a given hold time. The saturation behaviour is important for design considerations since hold times that follow it do not contribute to further damage [17-19]. Creep-fatigue life decreases with increasing tensile hold times due to the interaction between surface-initiated fatigue cracks and interior creep cavitation damage developed at grain boundaries and also, increasing the strain range results in decreasing the creep-fatigue life of the alloy due to the increase in corresponding stress amplitude, during which the critical crack length for failure decreases.

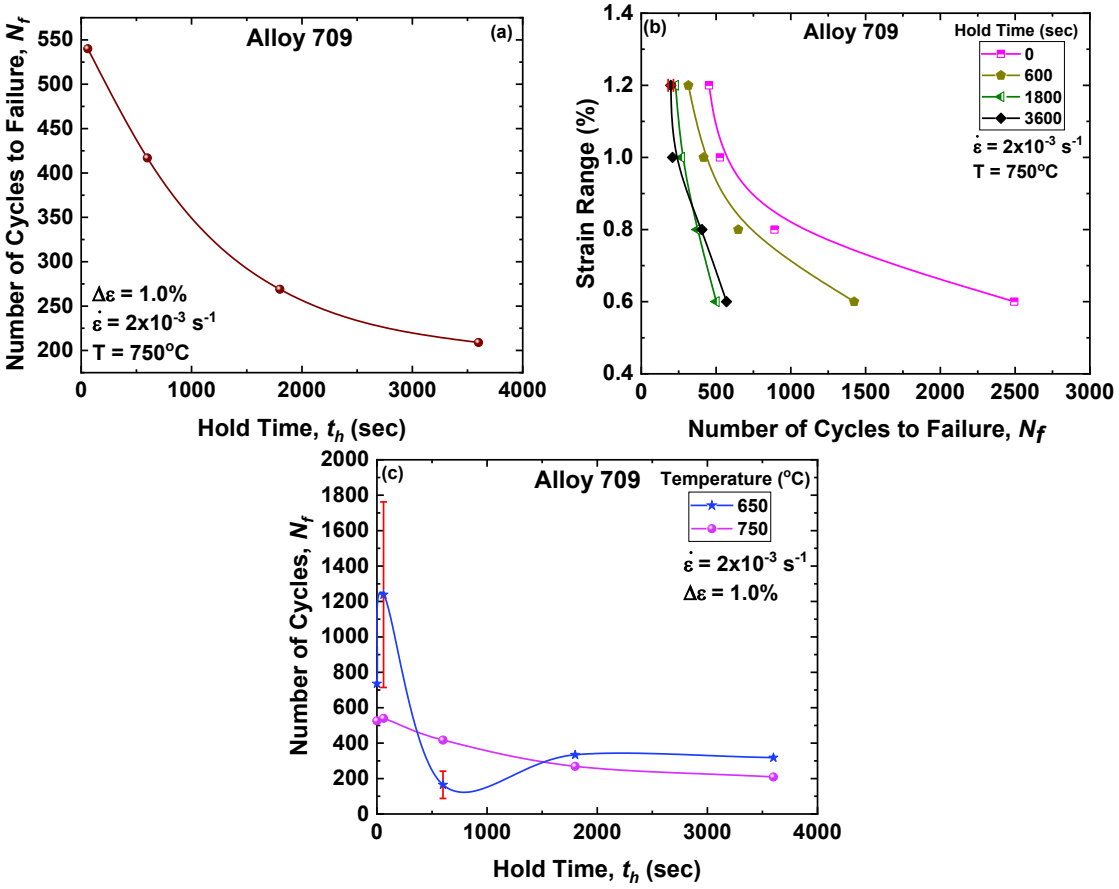


FIG.7 Creep-fatigue life of the Alloy 709 at different hold times (a), strain ranges (b) and temperatures (c).

### 3.2.2. Creep-Fatigue Interaction Diagram

According to the ASME Code, Section III, Subsection NH, constructing and plotting the creep-fatigue interaction diagram of the Alloy 709 is established following the linear damage summation (LDS). The linear damage summation rule is applicable over a wide variety of conditions with the availability of application data, and it is used to recognize which damage developed more rapidly until fracture. The creep-fatigue criterion is given by [17-19]:

$$\sum_j \left[\frac{n}{N_d}\right] + \sum_k \left[\frac{\Delta t}{T_d}\right] \le \boldsymbol{D} \qquad (4)$$

where $n$ and $N_d$ are the cycle number of type $j$ and the permissible cycles number of type $j$, respectively, and $\Delta t$ and $T_d$ are the actual time at stress level $k$ and the permissible time at the same stress level, respectively, and $D$ is the permissible combined damage fraction and it usually equals one. Creep damage fraction is determined using time-fraction method based on a linear correlation between the rupture time ($t$), temperature ($T$), and applied stress ($\sigma$) using Larson-Miller Parameter (LMP) and a power-law integration of the stress relaxation curve. Therefore, creep damage is calculated as following [17-19]:

$$D_k^c = \frac{b_o^{-m}}{A\left(1-b_1 m\right)}\left(\left(t_h + t_o\right)^{1-b_1 m} - \left(t_o\right)^{1-b_1 m}\right) \tag{5}$$

where $t_h$ is the stress relaxation hold time in seconds, $A$ and $m$ are fitting parameters in the LMP as a function of stress and $b_o$, $t_o$ and $b_1$ are fitting parameters in the power-law integration of the stress relaxation curve. More details are found in the work of Alsmadi, et al. [17-19]. FIG.8 depicts the creep-fatigue interaction diagram of the Alloy 709 plotted at different hold times, strain ranges and temperatures, where creep damage is plotted as function of fatigue damage. As shown, both fatigue and creep damages decrease with increasing the hold time, in which data points lie above and below the ideal failure criterion. Data points lying above the ideal failure criterion represent a strong creep-fatigue interaction, while the ones lying below it may represent a weak creep-fatigue interaction. Furthermore, high values of creep damage means that cavitation damage is enhanced by cyclic loading, while high values of fatigue damage means that crack propagation is enhanced by cavitation damage. The creep–fatigue damage envelope elucidates the average trend of the interaction between creep and fatigue damages depending on the material and the microstructure [17-19].

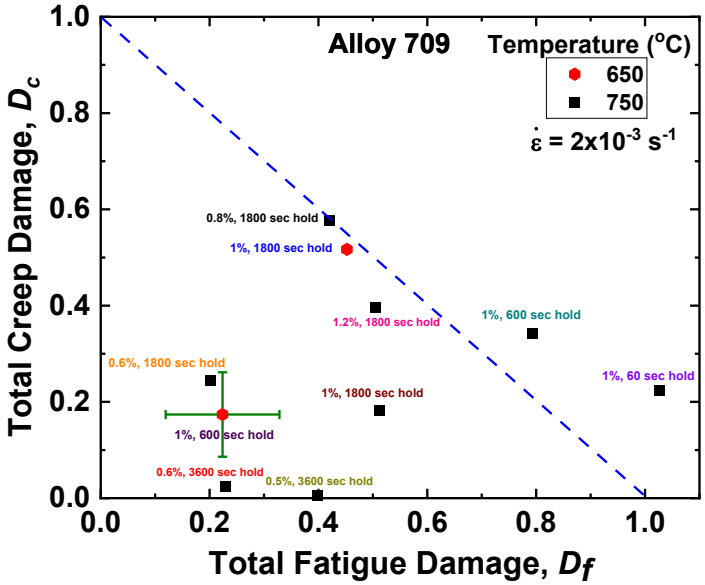


FIG. 8 Creep-fatigue interaction diagram of the Alloy 709 at at different hold times, strain ranges and temperatures.

### 3.2.3. Microstructural Characterization of The Alloy 709

Creep-fatigue deformation is a combination of creep deformation and fatigue deformation and is described as a mixed mode crack growth of pure transgranular fatigue cracks and intergranular creep cavities developing independently on the grain boundaries. FIG.9a shows the fractographs of the fracture surface of the Alloy 709 under low-cycle fatigue (LCF) damage (no hold time) at 1.0% strain range and 750 °C using scanning electron microscopy (SEM), while FIG.9b shows the fractographs of the Alloy 709 under creep-fatigue damage at 1.0% strain range and 60 seconds hold time at 750 °C. In pure fatigue tests (FIG.9a), high density of fatigue striations is observed due to crack propagation indicating that fatigue is the dominant damage mode. On the other hand, striations start to disappear with increasing hold time under creep-fatigue tests indicating that the dominant damage mode is comprised of both creep and fatigue damages. Also, the density of creep cavities (red circles)

increases with increasing hold time where they are observed at grain boundaries. In creep-fatigue damage, cracking mode changes from mixed mode (intergranular and transgranular) to intergranular mode with increasing hold time, where intergranular cracks (white arrows) become more dominant than the transgranular cracks (red arrows).

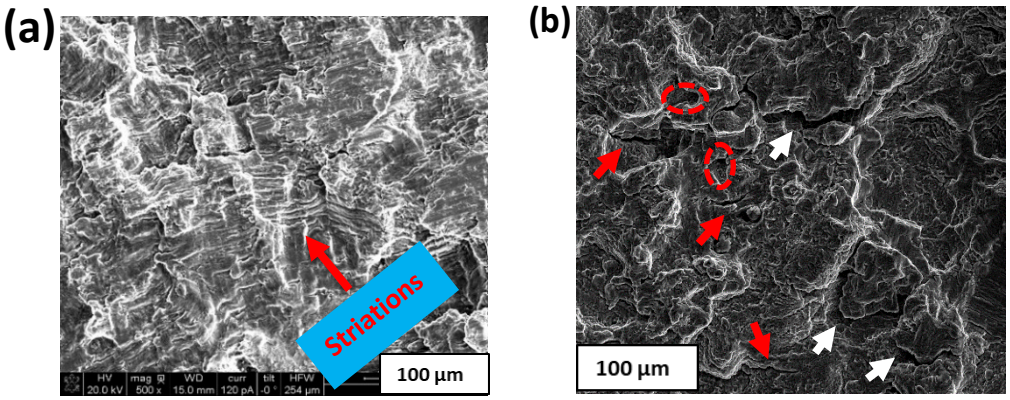


FIG.9 Fractographs of the fracture surface of the Alloy 709 under low-cycle fatigue (LCF) (no hold time) (a) and creep-fatigue at 60 seconds hold time (b). Both at 750 ºC and 1.0% strain range.

## 4. CONCLUSION

Creep behaviour in terms of creep curves characterises and deformation mechanisms were examined for the advanced austenitic stainless-steel Alloy 709 (Fe-25wt.%Ni-20%Cr) at temperatures and stresses from 700 – 800 °C and 40 – 275 MPa, respectively. The following conclusion were made:

- Typical creep curves exhibiting the three regimes of primary, steady state and tertiary creep regimes were usually observed in the Alloy 709.
- The minimum creep rate was found to increases with temperature and applied stress.
- The average values of the stress exponent and activation energy for creep were found to be 7.1 ± 0.6 and 446 kJ/mole, respectively.
- Based on the indicative creep parameters, dislocation creep was inferred to be the rate controlling creep mechanism.
- The Alloy 709 was found to follow Monkman-Grant relation of $\dot{\varepsilon}_m^{\alpha}\ t_f = C_{MG}$, where α and C are determined to be close to 1 and 0.1, respectively.
- Larson– Miller parameter (LM) for the Alloy 709 was established and the temperatures in K for 100,000 hours rupture life using LMP was estimated.

Strain-controlled creep-fatigue tests were performed on the Alloy 709 at 650 °C and 750 °C and $2\times10^{-3}$ $s^{-1}$ strain rate with strain ranging from 0.3% to 1.2% and tensile hold times of 0, 60, 600, 1,800, and 3,600 seconds. The following conclusion were made:

- The creep-fatigue life of the Alloy 709 was found to decrease with increasing hold time, strain range and temperature until saturation.
- The creep-fatigue interaction diagram of the Alloy 709 was plotted according to the ASME Code, Section III, Subsection NH, following the linear damage summation (LDS), at different hold times, strain ranges and temperatures.
- Both fatigue and creep damages decreased with increasing the hold time, in which data points lie above the ideal failure criterion represent a strong creep-fatigue interaction, while the ones lying below it may represent a weak creep-fatigue interaction.
- The creep–fatigue damage interaction diagram explains the average trend of the interaction between creep and fatigue damages depending on the material and the microstructure.

- In pure fatigue tests, transgranular fatigue cracks are the dominant damage mode while in creep-fatigue tests, the dominant damage mode is comprised of both intergranular creep cavities and transgranular fatigue cracks.

## ACKNOWLEDGEMENTS

The authors gratefully acknowledge the financial support from the Nuclear Energy University Programs (NEUP/ Project #15-8582) of the Department of Energy, Office of Nuclear Energy for performing this research, and Dr. Sam Sham of Argonne National Laboratory for supplying the experimental material and support and discussions. The authors would also like to acknowledge the use of microscopy facility at Advanced Instrumentation Facility and the use of optical microscopy at the Industrial and Systems Engineering at North Carolina State University, Raleigh, USA. AA is thankful to KACST for funding of his doctoral degree studies.

## REFERENCES

[1] D. Buckthorpe, Ch1 - Introduction to Generation IV nuclear reactors, in: P. Yvon (Ed.), Structural Materials for Generation IV Nuclear Reactors, Woodhead Publishing2017, pp. 1-22.
[2] S.J. Zinkle, J.T. Busby, Structural materials for fission & fusion energy, Materials Today 12(11) (2009) 12-19.
[3] F. Dalle, M. Blat-Yrieix, S. Dubiez-Le Goff, C. Cabet, P. Dubuisson, Ch17 - Conventional austenitic steels as out-of-core materials for Generation IV nuclear reactors, in: P. Yvon (Ed.), Structural Materials for Generation IV Nuclear Reactors, Woodhead Publishing2017, pp. 595-633.
[4] W. Hoffelner, Materials for Nuclear Plants From Safe Design to Residual Life Assessments, Springer, Switzerland2013.
[5] K.L. Murty, I. Charit, Structural materials for Gen-IV nuclear reactors: Challenges and opportunities, Journal of Nuclear Materials 383(1) (2008) 189-195.
[6] P.J. Maziasz, J.P. Shingledecker, N.D. Evans, Y. Yamamoto, K.L. More, R. Trejo, E. Lara-Curzio, Creep Strength and Microstructure of AL20-25+Nb Alloy Sheets and Foils for Advanced Microturbine Recuperators, Journal of Engineering for Gas Turbines and Power 129(3) (2006) 798-805.
[7] W. Corwin, Advanced Structural Materials (RC-3), Nuclear Energy University Programs (NEUP), Fiscal Year (FY) 2015 Annual Planning Webinar, DOE, 2014.
[8] T.-L. Sham, K. Natesan, Code Qualification Plan for an Advanced Austenitic Stainless Steel, Alloy 709, for Sodium Fast Reactor Structural Applications, International Conference on Fast Reactors and Related Fuel Cycles: Next Generation Nuclear Systems for Sustainable Development (FR17), IAEA, Yekaterinburg, Russian Federation, 2017.
[9] P.J. Maziasz, Development of Creep-Resistant and Oxidation-Resistant Austenitic Stainless Steels for High Temperature Applications, JOM 70(1) (2018) 66-75.
[10] X. Zhang, T.-L. Sham, FY19 Status Report on Creep Test Data on Commercial Heat of Alloy 790, Argonne National Laboratory, 2019.
[11] A.S. Alomari, N. Kumar, K.L. Murty, Serrated yielding in an advanced stainless steel Fe-25Ni-20Cr (wt%), Materials Science and Engineering: A 751 (2019) 292-302.
[12] A.S. Alomari, N. Kumar, K.L. Murty, Enhanced ductility in dynamic strain aging regime in a Fe-25Ni-20Cr austenitic stainless steel, Materials Science and Engineering: A 729 (2018) 157-160.
[13] S. Upadhayay, H. Li, P. Bowen, A. Rabiei, A study on tensile properties of Alloy 709 at various temperatures, Materials Science and Engineering: A 733 (2018) 338-349.
[14] R. Ding, J. Yan, H. Li, S. Yu, A. Rabiei, P. Bowen, Deformation microstructure and tensile properties of Alloy 709 at different temperatures, Materials & Design 176 (2019) 107843.
[15] Y. Zhao, M.N. Cinbiz, J.-S. Park, J. Almer, D. Kaoumi, Tensile behavior and microstructural evolution of a Fe-25Ni-20Cr austenitic stainless steel (alloy 709) from room to elevated temperatures through in-situ synchrotron X-ray diffraction characterization and transmission electron microscopy, Journal of Nuclear Materials 540 (2020) 152367.
[16] A.S. Alomari, N. Kumar, K.L. Murty, Creep Behavior and Microstructural Evolution of a Fe-20Cr-25Ni (Mass Percent) Austenitic Stainless Steel (Alloy 709) at Elevated Temperatures, Metallurgical and Materials Transactions A 50(2) (2019) 641-654.
[17] Z.Y. Alsmadi, A. Alomari, N. Kumar, K.L. Murty, Effect of hold time on high temperature creep-fatigue behavior of Fe–25Ni–20Cr (wt.%) austenitic stainless steel (Alloy 709), Materials Science and Engineering: A 771 (2020) 138591.
[18] Zeinab Y. Alsmadi, K.L. Murty, Effect of Strain Range on High Temperature Creep-Fatigue Behavior of Fe-25Ni-20Cr (wt.%) Austenitic Stainless Steel (Alloy 709), Materials at High Temperatures, 38:1, pp. 47-60, (2021).
[19] Zeinab Y. Alsmadi, K.L. Murty, High-temperature effects on creep-fatigue interaction of the Alloy 709 austenitic stainless steel, International Journal of Fatigue, vol. 143, 105987 (2021).

[20] A. Lall, S. Sarkar, R. Ding, P. Bowen, A. Rabiei, Performance of Alloy 709 under creep-fatigue at various dwell times, Materials Science and Engineering: A 761 (2019) 138028.
[21] T.D. Porter, K.O. Findley, M.J. Kaufman, R.N. Wright, Assessment of creep-fatigue behavior, deformation mechanisms, and microstructural evolution of alloy 709 under accelerated conditions, International Journal of Fatigue 124 (2019) 205-216.
[22] N. Shaber, R. Stephens, J. Ramirez, G.P. Potirniche, M. Taylor, I. Charit, H. Pugesek, Fatigue and creep-fatigue crack growth in alloy 709 at elevated temperatures, Materials at High Temperatures 36(6) (2019) 562-574.
[23] M. Taylor, J. Ramirez, I. Charit, G.P. Potirniche, R. Stephens, M.V. Glazoff, Creep behavior of Alloy 709 at 700 °C, Materials Science and Engineering: A 762 (2019) 138083.
[24] T. Chen, Y. Yang, L. He, B. Tyburska-Püschel, K. Sridharan, H. Xu, L. Tan, Enhanced diffusion of Cr in 20Cr-25Ni type alloys under proton irradiation at 670 °C, Nuclear Materials and Energy 17 (2018) 142-146.
[25] R. Ding, J. Yan, H. Li, S. Yu, A. Rabiei, P. Bowen, Microstructural evolution of Alloy 709 during aging, Materials Characterization 154 (2019) 400-423.
[26] T. Sourmail, H. Bhadeshia, Microstructural evolution in two variants of NF709 at 1023 and 1073 K, Metallurgical and Materials Transactions A-physical Metallurgy and Materials Science - METALL MATER TRANS A 36 (2005) 23-34.
[27] X. Zhang, W.-Y. Chen, A. Caputo, In-situ ion irradiation study of alloy 709 stainless steels with different processing histories, Journal of Nuclear Materials 553 (2021) 153052.
[28] S.J. Reese, D.S. Smith, R.E. Rupp, J.K. Wright, A.R. Khanolkar, R.N. Wright, D.H. Hurley, Elevated-Temperature Elastic Properties of Alloys 709 and 617 Measured by Laser Ultrasound, Journal of Materials Engineering and Performance 30(2) (2021) 1513-1520.
[29] D.S. Smith, N.J. Lybeck, J.K. Wright, R.N. Wright, Thermophysical properties of Alloy 709, Nuclear Engineering and Design 322 (2017) 331-335.
[30] S. Sham, K. Natesan, Code Qualification Plan for an Advanced Austenitic Stainless Steel, Alloy 709, for Sodium Fast Reactor Structural Applications, 2017.